Response to Referee #1

We sincerely thank the referee for their careful reading of our manuscript and for their constructive comments and suggestions. Their feedback has been very helpful in improving the clarity and quality of the paper. Below, we provide a point-by-point response to each comment, with the referee's remarks reproduced for clarity followed by our replies.

R.C. 1.1: Figure 5 labels the x-axis in Hz (frequency domain), while Figure 15 uses cm^{-1} (wavenumber domain) without justification. This inconsistency requires clarification or standardization.

A.C.:

We thank the referee for carefully noting the inconsistency in the axis labeling between Figures 5 (likely referring to Figure 6(c)) and Figure 15. We acknowledge this oversight and sincerely apologize for the confusion it may have caused. For clarification, the x-axis in these FFT plots was generated from the Fourier transform of the residual difference between the calculated and measured spectra. Since the spectral grid is defined in wavenumber (cm^{-1}), the spectral spacing determines the Fourier transform frequency axis, whose correct unit is cycles per cm^{-1}. In the original submission, this was mistakenly labeled as "Hz" in Figures 6(c) and as "cm^{-1}" in Figure 15. We have now corrected the labeling throughout the manuscript to "cycles per cm^{-1}," ensuring consistency. This correction does not affect the results or conclusions of the study but only rectifies the figure labels.

R.C. 1.2: Figure 12 (temporal evolution of FTIR transmission spectra) is not cited or discussed in the main text, leaving its relevance unclear.

A.C.:

Figure 12 has now been explicitly cited and discussed in Section 4 of the revised manuscript. Its purpose is to illustrate the temporal degradation of the instrument response by comparing background and HBr transmission spectra across different measurement dates. The background spectra (Fig. 12a) reveal progressive loss of source intensity and growing baseline instability, while the HBr spectra (Fig. 12b) highlight the cumulative influence of retroreflector misalignment, baseline drift, and channeling artifacts on absorption features. By including these spectra, we aim to demonstrate the broader impact of long-term instrumental degradation on both the continuum and gas-specific signatures, thereby providing essential context for the subsequent ILS retrieval and residual analyses (Figs. 13–15). This clarification has been added to the text to ensure that the relevance of Figure 12 is clear to readers.

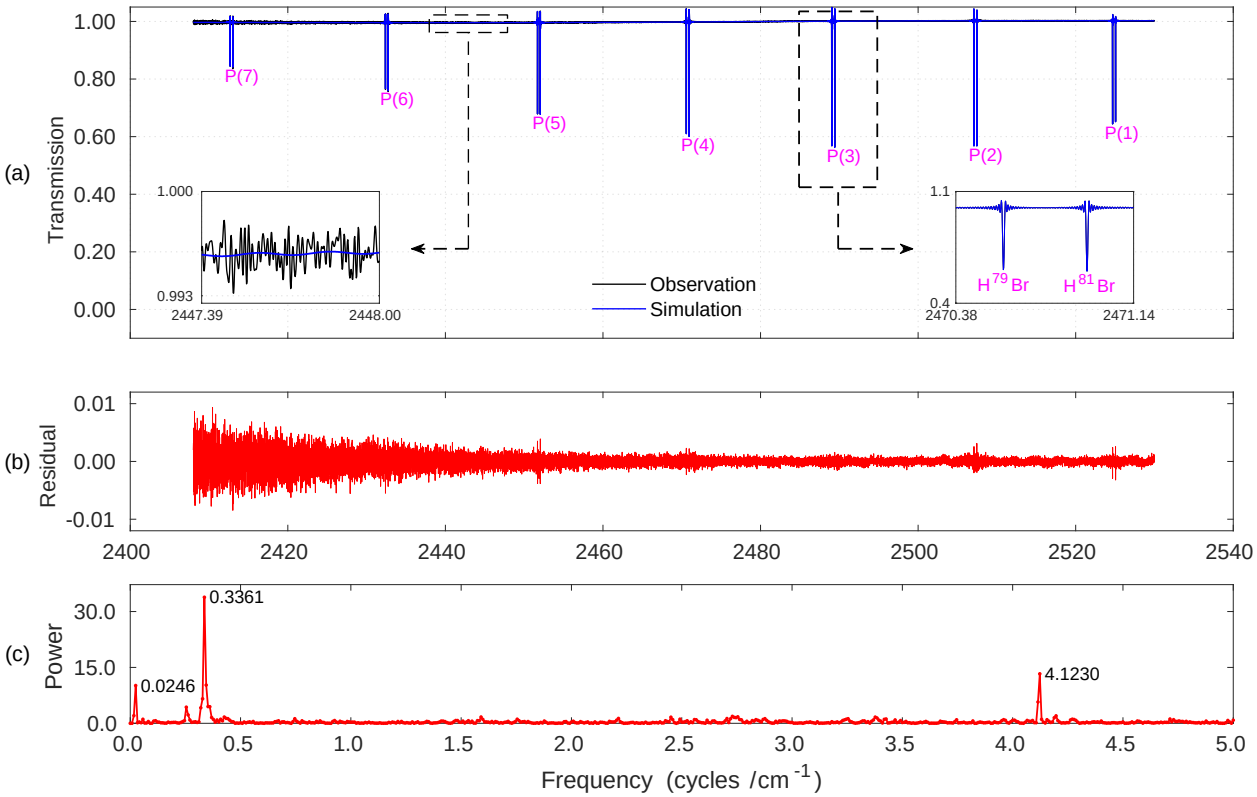

Figure 6. HBr transmission spectra acquired via gas cell measurement. (a) Comparison between observed and simulated spectra in the region 2400-2540 cm^{-1}, illustrating P-branch transitions. Insets display isotopic splitting (right) and low-amplitude channeling patterns (left). (b) Residuals between experiment and simulation. (c) FFT of the residual showing dominant frequencies linked to channeling artifacts arising from instrumental imperfections. Data acquired on December 14^{th}, 2012.

R.C. 1.3: The manuscript alternates between "Figure" (e.g., Section 4) and "Fig." (e.g., Section 2.2.1) for figure references. A uniform style should be adopted.

A.C.:

We have revised the manuscript to ensure consistency, and all figure references have now been changed to "Fig." throughout the text.

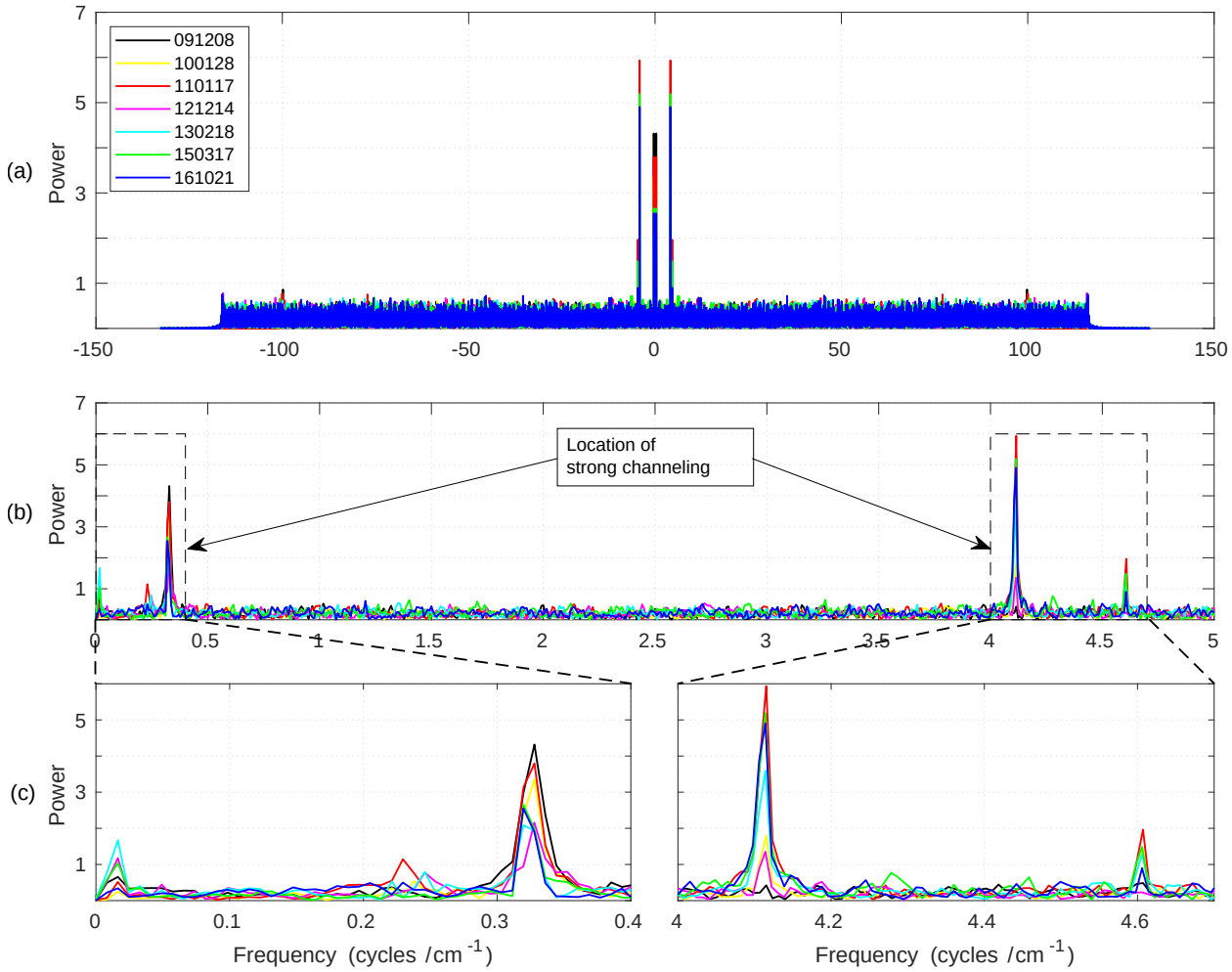

Figure 15. Initial guess of the channeling locations based on long-term spectral channeling behavior of the Bruker FTS 120M spectrometer at Addis Ababa, illustrating evolving frequencies. (a) Double-sided FFT of the residual difference between measured and nominally simulated spectra. (b) Single-sided spectrum emphasizing the low-frequency region (0–5 cycles/cm^{-1}). (c) Magnified views of the boxed regions in (b) around 0–0.4 cycles/cm^{-1} (left) and 4–4.7 cycles/cm^{-1} (right), highlighting the spectral fingerprints of strong channeling.

R.C. 1.4: The methodology for computing the ILS averaging kernel in Figure 16 is not described, including whether it derives from LINEFIT retrievals or ALIGN60 simulations.

A.C.:

The general procedure for ILS retrieval has already been described in the manuscript and summarized in the workflow figure (Figure 7). Specifically, the ILS was retrieved with LINEFIT through nonlinear fitting of HBr cell spectra, simultaneously optimizing instrumental and spectroscopic parameters including cell temperature, column amount, frequency shift, ILS amplitude and phase, baseline, and channeling contributions. During the iterative fitting process, the Jacobian matrix of these parameters is computed, and

from this the ILS averaging kernel is constructed. This kernel quantifies the sensitivity of the retrieval along the interferometer scan path. Thus, any deviation of the kernel from nominal behavior reflects perturbations in the retrieved parameters, which can be attributed to mechanical shear misalignments or artifacts of electronic and optical origin. Once convergence is reached, LINEFIT provides the ILS averaging kernel as part of its standard output, thereby directly representing the sensitivity of the instrument characterization. Importantly, Figure 16 provides immediate insight into instrument performance, as the structure and deviations of the kernel illustrate how well the interferometer behaves relative to nominal alignment and stability. For further methodological details, we refer the referee to the standard descriptions in Hase (2012); Garc'ia et al. (2022), which underpin the ILS retrieval procedure applied in this work.

R.C. 1.5: Channeling frequencies listed in Table 3 (e.g., 2.9750 cm^{-1}) are not explicitly mapped to the FFT peaks in Figure 15, creating ambiguity in their correlation.

A.C.:

We thank the referee for raising this important point regarding the mapping of channeling frequencies. In the NDACC community, it is standard practice to report channeling frequencies in units of cm^{-1} (e.g.,Blumenstock et al. (2021)). To ensure consistency with this tradition, we have revised the frequency representation accordingly. As clarified under R.C. 1.1, the labeling of Figure 15 has been corrected so that the FFT axis is expressed in cycles per cm^{-1}. To harmonize with NDACC reporting practice, the corresponding values in Table 3 are reported in cm^{-1} by applying the reciprocal relationship:

$$\text{channeling frequency}\,[\text{cm}^{-1}] = \frac{1}{f\,[\text{cycles per cm}^{-1}]}.$$

For example, the dominant FFT peak at $f = 0.3361$ cycles per cm^{-1} in Figure 15 corresponds to a channeling frequency of about 2.9750 cm^{-1}, which is listed in Table 3. All frequency values in Table 3 were derived consistently in this manner. We have clarified this in Section 3.8 and in the captions of Figure 15 and Table 3, making the connection between FFT peaks and tabulated values explicit, while also ensuring consistency with NDACC reporting conventions.

R.C. 1.6: Residuals in Figure 14 appear identical for "Nominal" (absolute values) and "Modified" (percentage), undermining direct comparison. Figure 13 similarly lacks clarity in residual scaling.

A.C.:

We appreciate the referee's careful reading of the manuscript and fully recognize that the original presentation of residuals could be misinterpreted due to inconsistent scaling between the nominal and modified configurations. In the earlier version, the residuals associated with the P(6) line were expressed as relative percentage deviations for the modified configuration, whereas the nominal configuration employed absolute residuals. This inconsistency could indeed obscure genuine differences between the two cases and thereby weaken the interpretability of the comparison. In the revised manuscript, we have resolved this issue comprehensively, together with several important improvements detailed below.

To improve the diagnostic sensitivity of the residual analysis, we have replaced the previously illustrated P(6) line with the higher-SNR P(2) transition of HBr. This line sits in a region of significantly reduced

noise and exhibits clearer, well-defined systematic residual structures under the nominal configuration. Because these structures are more diagnostic of ILS distortions, P(2) provides a more sensitive basis for evaluating and demonstrating the benefit of the modified configuration. This change also ensures coherence throughout the manuscript, as P(2) is widely used in NDACC-standard ILS characterization and is better suited for illustrating instrumental improvements.

In the original manuscript, Figure 14 showed the modified residuals in percentage units while the nominal residuals appeared in absolute units, creating an unintended mismatch that hindered direct comparison. In the revised version, the P(2) line is now used and all residuals — nominal, modified, and their differences — are plotted in absolute transmission units, with the $\times 10^{-3}$ A.U. scaling factor explicitly annotated on the axes. This uniform representation allows the magnitude and structure of residuals to be interpreted clearly and consistently, making the reduction in systematic residual features under the modified configuration immediately evident.

Likewise, the previous version of Figure 13 lacked explicit scaling information for the plotted residual metrics and presented numerical performance indicators with inconsistent precision. In the revised manuscript, all residual-related panels in Figure 13 now clearly indicate the $\times 10^{-2}$ A.U. scaling, and both the nominal and modified configurations are displayed using the same absolute residual units. Furthermore, all performance statistics shown on the figure — σ, RMS, MAE, residual range, and maximum residual — are now reported to three significant figures, ensuring clarity and consistency across datasets and eliminating any impression of artificial precision.

Example plots corresponding to the revised Figure 13 and Figure 14 (showing the updated residual scaling and the P(2) transition) are provided below for the referee's reference.

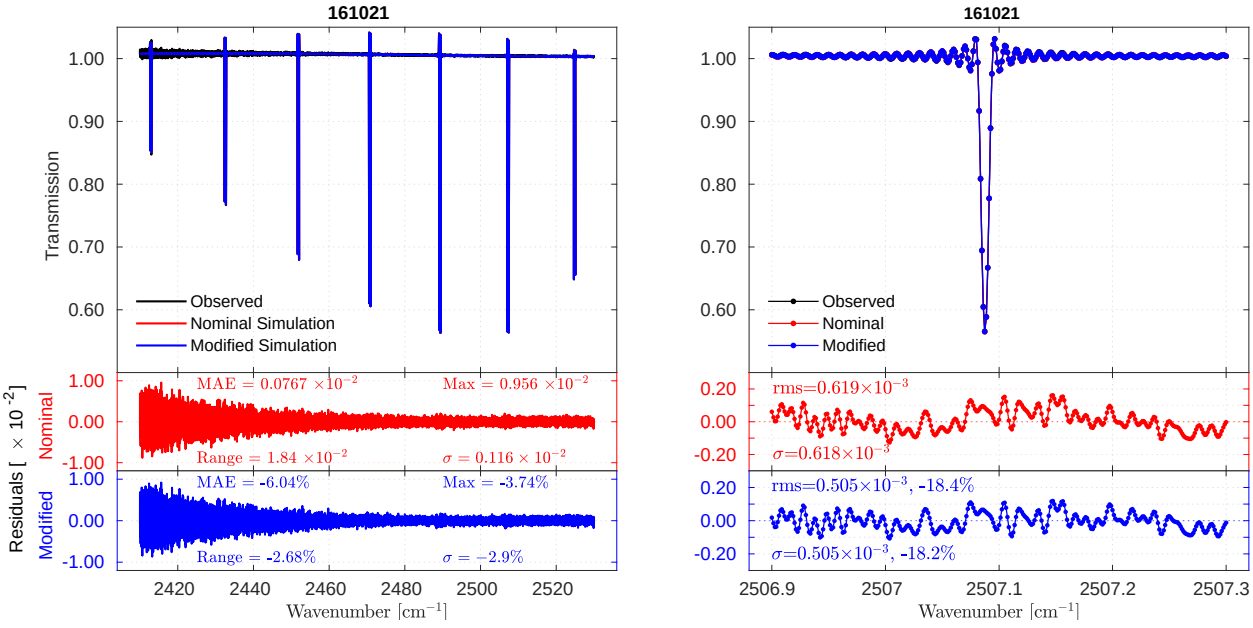

Figure 13 (left) and **Figure 14** (right).

R.C. 1.7: The cited RMS range (3.7×10^{-3} to 5.04×10^{-3}) does not match the values displayed in Figure 14's residual plots, necessitating verification.

A.C.:

We thank the referee for carefully pointing out this inconsistency. The discrepancy arose because the RMS values were mistakenly taken from the *modified configuration*, expressed in absolute terms (3.72% to 5.04%), rather than from the *nominal configuration* associated with the residual plots in Figure 14. We sincerely apologize for this oversight. The correct RMS values corresponding to the nominal configuration are 0.49×10^{-3} **to** 0.666×10^{-3}. We have corrected this in the revised manuscript.

- **Section 4: Results and Data Analysis (pages 24–25)** — In the discussion of Figure 14 (middle panels), the sentence currently reading:

  > "...with σ values ranging from 1.36 $\times$ 10^{-3} to 1.83 $\times$ 10^{-3} and rms values from 3.70 $\times$ 10^{-3} to 5.04 $\times$ 10^{-3} (Figure 14, middle panels)."

  has been corrected to:

  > "...with σ values ranging from 0.49×10^{-3} to 0.666×10^{-3} and rms values from 0.491×10^{-3} to 0.67×10^{-3} (Figure 14, middle panels)."

- **Section 5: Discussion (page 27)** — Where the RMS values are again cited in relation to the performance comparison, the text has been updated to reflect the correct nominal RMS range (0.491×10^{-3} to 0.67×10^{-3}), ensuring consistency across both sections.

We appreciate the referee's careful reading, which has helped us improve both the accuracy and clarity of the manuscript.

R.C. 1.8: While ILS improvements are shown, there is minimal validation of how these translate to more accurate retrievals of key atmospheric trace gases (e.g., CO, C_2H_6). Concrete examples linking ILS metrics to retrieval errors would strengthen relevance.

A.C.:

We sincerely thank the reviewer for highlighting the importance of connecting the improvements in ILS characterization to their influence on atmospheric retrieval accuracy. We fully agree that demonstrating how the corrected non-ideal instrumental effects propagate into retrievals of key trace gases such as CO and C_2H_6 is essential for emphasizing the broader relevance of this work.

At the same time, we would like to clarify that the present manuscript is the first part of a structured two-paper sequence. Its primary objective is to rigorously diagnose, quantify, and correct non-ideal instrumental effects using HBr cell measurements, ALIGN60 simulations, and LINEFIT retrievals. Incorporating a complete atmospheric retrieval assessment here would significantly expand the length and shift the focus away from the core purpose of this study, which is to establish a validated instrumental performance framework.

The atmospheric validation requested by the reviewer is not omitted; rather, it is treated comprehensively in a dedicated companion manuscript titled *"Non-Ideal Instrumental Impacts on the Abundance and*

Uncertainty of CO, C_2H_6, HCN, and C_2H_2 Retrieved from High-Resolution Ground-Based FTIR". This second paper uses the empirically corrected ILS parameters derived here to compute long-term PROFFIT retrievals (2009–2017) for NDACC-standard microwindows over Addis Ababa. It presents a detailed comparison of retrievals using nominal versus modified configurations in terms of:

- Retrieval accuracy and uncertainty budgets,
- Vertical sensitivity and averaging kernel behaviour,
- Partial and total column differences,
- Vertical resolution changes, and
- Compensation versus non-compensation effects across atmospheric layers.

Therefore, the present manuscript focuses on establishing a rigorous experimental and diagnostic framework for characterizing and correcting non-ideal instrumental effects, while the companion manuscript applies these empirical corrections directly to atmospheric retrievals of CO, C_2H_6, HCN, and C_2H_2, and evaluates their impacts on retrieval accuracy, sensitivity, resolution, and uncertainty. Together, the two manuscripts are intentionally designed to be coherent, complementary, and appropriately scoped: the current paper addresses instrument performance characterization, and the companion paper addresses its atmospheric implications.

R.C. 1.9: The paper lacks a detailed flowchart or step-by-step workflow for ALIGN60 and LINEFIT procedures. A visual schema would enhance reproducibility, especially for non-specialists.

A.C.:

In the revised version of the manuscript, we have now added a comprehensive workflow figure (Figure 7) that illustrates the sequential steps for both ALIGN60 and LINEFIT. The schema starts from the preprocessing of the HBr transmission spectra and configuration of nominal instrument parameters, through the retrieval of HBr cell parameters and the retrieval of both nominal and non-ideal ILS in LINEFIT. On the ALIGN60 side, the workflow presents the input configuration, initialization of the constant shear, iterative adjustment of linear and periodic shear components, and validation against Haidinger fringes. We further clarify in the revised text that the initial constant shear is set according to the reference value provided by Sun et al. (2018), and then iteratively tuned. The direction and magnitude of the adjustment are determined by the degree of agreement between ALIGN60 and LINEFIT ILS, using the RMS of their difference as the optimization criterion. Once convergence is reached, the resulting ILS and Haidinger fringes are considered representative of the instrument performance. We believe that the addition of this workflow figure, together with these methodological clarifications, significantly improves the accessibility and reproducibility of the procedures.

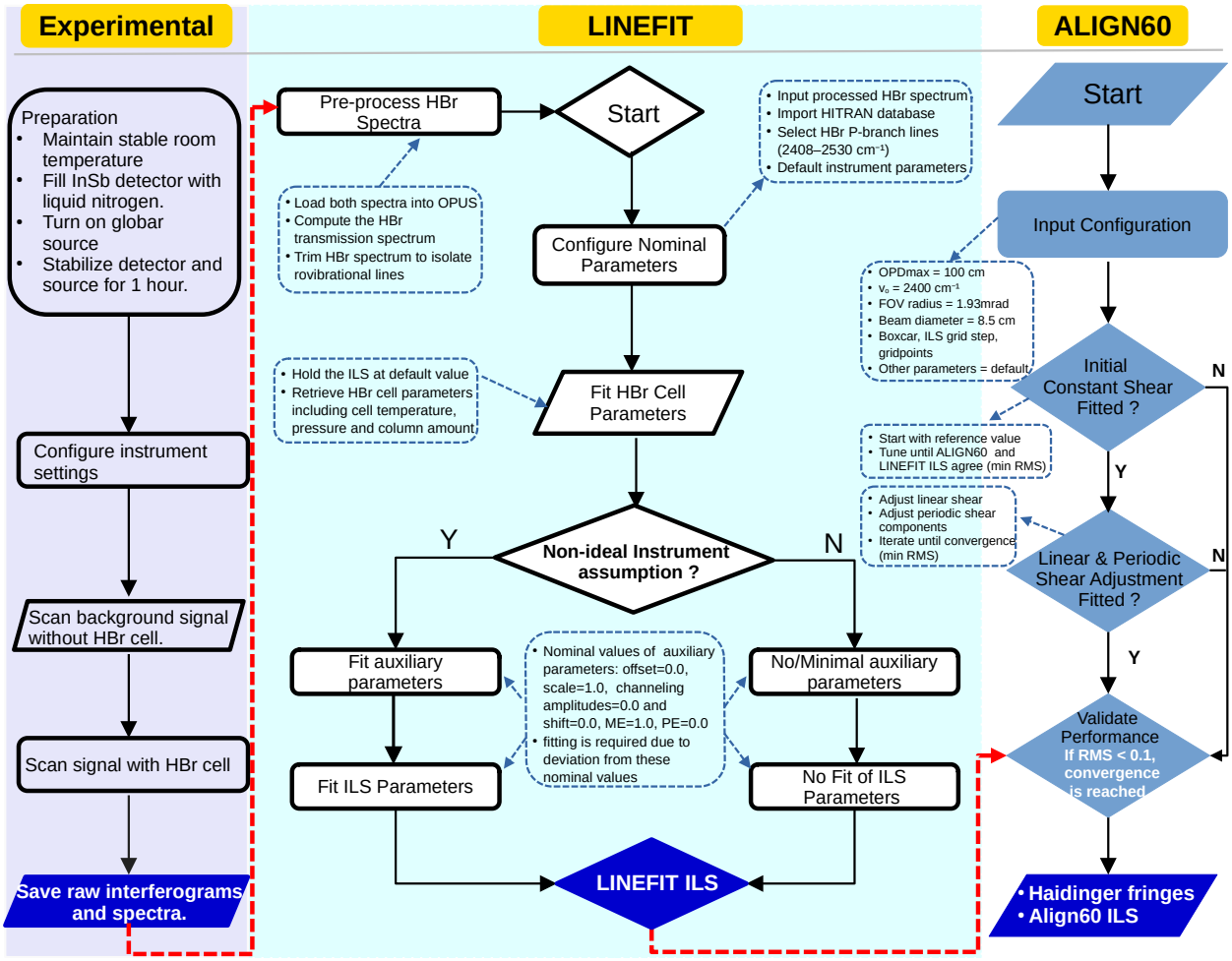

Figure 7. Workflow for Instrumental Characterization: integrating experimental setup, data Processing with LINEFIT and ALIGN60, and iterative optimization for ILS and Haidinger Fringe Simulations.

References

Thomas Blumenstock, Frank Hase, Axel Keens, Denis Czurlok, Orfeo Colebatch, Omaira Garcia, David WT Griffith, Michel Grutter, James W Hannigan, Pauli Heikkinen, et al. Characterization and potential for reducing optical resonances in fourier transform infrared spectrometers of the network for the detection of atmospheric composition change (ndacc). *Atmospheric Measurement Techniques*, 14(2):1239–1252, 2021.

Omaira E Garc'ia, Esther Sanrom'a, Frank Hase, Matthias Schneider, Sergio Fabi'an Le'on-Luis, Thomas Blumenstock, Eliezer Sep'ulveda, Carlos Torres, Natalia Prats, Alberto Redondas, et al. Impact of instrumental line shape characterization on ozone monitoring by ftir spectrometry. *Atmospheric Measurement Techniques*, 15(15):4547–4567, 2022.

F Hase. Improved instrumental line shape monitoring for the ground-based, high-resolution ftir spectrometers of the network for the detection of atmospheric composition change. *Atmospheric Measurement Techniques*, 5(3):603–610, 2012.

Youwen Sun, Mathias Palm, Cheng Liu, Frank Hase, David Griffith, Christine Weinzierl, Christof Petri, Wei Wang, and Justus Notholt. The influence of instrumental line shape degradation on ndacc gas retrievals: total column and profile. *Atmospheric Measurement Techniques*, 11(5):2879–2896, 2018.